ADVANCED HEALTHCARE MATERIALS
www.advhealthmat.de

Cephalopod-Inspired Miniaturized Suction Cups for Smart Medical Skin

*Moon Kee Choi, Ok Kyu Park, Changsoon Choi, Shutao Qiao, Roozbeh Ghaffari, Jaemin Kim, Dong Jun Lee, Myungbin Kim, Wonji Hyun, Seok Joo Kim, Hye Jin Hwang, Seung-Hae Kwon, Taeghwan Hyeon, Nanshu Lu, and Dae-Hyeong Kim**

Nature has inspired important advances in the design of mechanical/chemical adhesives.[1–5] In particular, recent demonstrations of biomimetic dry adhesives based on gecko setae[6–9] and chemical glues derived from shellfish proteins[10] provide compelling routes for medical devices that must interface with skin and/or organs. The intimate interfacing is important,[11,12] since it oftentimes determines the wearability[13,14] and the quality of diagnosis and therapy.[15–20] Capabilities for the multiple regeneration of adhesives and the biocompatibility upon detachment from target skin/organ surfaces require more advanced technologies. However, robust, conformal contacts between medical electronics/therapeutics and curvilinear, textured surfaces of dynamically contorting skin remain challenging with existing packaged electronics and encapsulation strategies.[21–23]

Cephalopods (e.g., octopus and squid) provide an intriguing example in nature, whereby the arrayed geometry of suction cups and low modulus of the skin achieve robust and conformal adhesion without chemical adhesives.[24,25] Here, we present cephalopod-inspired miniaturized suction cup (mSC) dry adhesives that are combined with ultrathin stretchable electronics to create a new class of glue-free diagnosis and therapy system. The ultralow modulus (≈108 kPa) mSC array supports embedded stretchable electronics and drug-loaded therapeutic nanoparticles, while firmly laminating on skin without inducing skin irritations/damages during long-term usage and removal. The integrated system allows continuous monitoring of vital sign changes in various physiologic or pathophysiologic conditions, controllable release of drugs, and wireless communication from/to external devices for the remote healthcare. Strong van der Waals forces and negative pressure based on mSC structures create robust mechanical coupling with skin, which enables highly sensitive/accurate biometric sensing and effective transdermal drug delivery, while preserving the tackiness over many uses and drug reloading. These new adhesion features serve a powerful, low cost alternative to single use chemical adhesives.

A representative scenario in clinical applications is described in **Figure 1**, whereby the electronic patch is firmly laminated on skin and linked to a wrist band that contains a power supply, a controller, and short-range wireless data transmission unit (Figures S1–S3, Supporting Information). The mSCs (Figure 1c; atomic force microscopy (AFM) images) inspired by octopus tentacles (Figure 1b and inset; optic (left) and 3D laser scanner (right) image) generate negative pressure, which promote adherence to skin. The ultrathin form factor (<50 μm) coupled with low system-level modulus (≈108 kPa) provides comfort, enhanced skin integration, and breathability for daily wear. Integrated sensors (strain gauges, cardiac sensing electrodes, and temperature sensors) monitor physical activity, fine movement such as physiologic or pathologic tremors, and vital signs (e.g., body temperature, respiration, electrocardiogram (ECG), pulse, and blood pressure) (Figure 1a). The measured biosignals are wirelessly transmitted to external devices through a Bluetooth module located in the smart band (Figure 1d, left). Acute changes and significant abnormalities of vital signs from a wide array of pathophysiologic conditions are detected with the electronic patch in real time. Alerts that signal the need for urgent medical attention or prevention of life-threatening clinical events can be broadcasted to emergency medical service providers through wireless networks (Figure 1d, right). Iontophoresis electrode deliver electric fields through dermis to modulate transdermal delivery of drugs loaded in mesoporous silica (m-SiO_2) nanoparticles (inset of Figure 1a) by accelerating transport of ions and drug molecules (Figure 1e). Drugs can be

M. K. Choi, C. Choi, J. Kim, D. J. Lee, M. Kim, W. Hyun, S. J. Kim, Prof. T. Hyeon, Prof. D.-H. Kim
Center for Nanoparticle Research
Institute for Basic Science (IBS)
Seoul 151-742, Republic of Korea
E-mail: dkim98@snu.ac.kr

M. K. Choi, C. Choi, J. Kim, D. J. Lee, M. Kim, W. Hyun, S. J. Kim, Prof. T. Hyeon, Prof. D.-H. Kim
School of Chemical and Biological Engineering
Institute of Chemical Processes
Seoul National University
Seoul 151-742, Republic of Korea

O. K. Park, S.-H. Kwon
Division of Bio-imaging
Korea Basic Science Institute
Chun-Cheon 200-701, Republic of Korea

S. Qiao, Prof. N. Lu
Center for Mechanics of Solids
Structures and Materials
Department of Aerospace Engineering and Engineering Mechanics
Texas Materials Institute
University of Texas at Austin
210 E 24th St, Austin, TX 78712, USA

R. Ghaffari
MC10 Inc.
9 Camp St, Cambridge, MA 02140, USA

H. J. Hwang
Division of Cardiology
Beth Israel Deaconess Medical Center
Harvard Medical School, Boston, MA 02215, USA

DOI: 10.1002/adhm.201500285

ADVANCED HEALTHCARE MATERIALS
www.advhealthmat.de

Materials Views
www.MaterialsViews.com

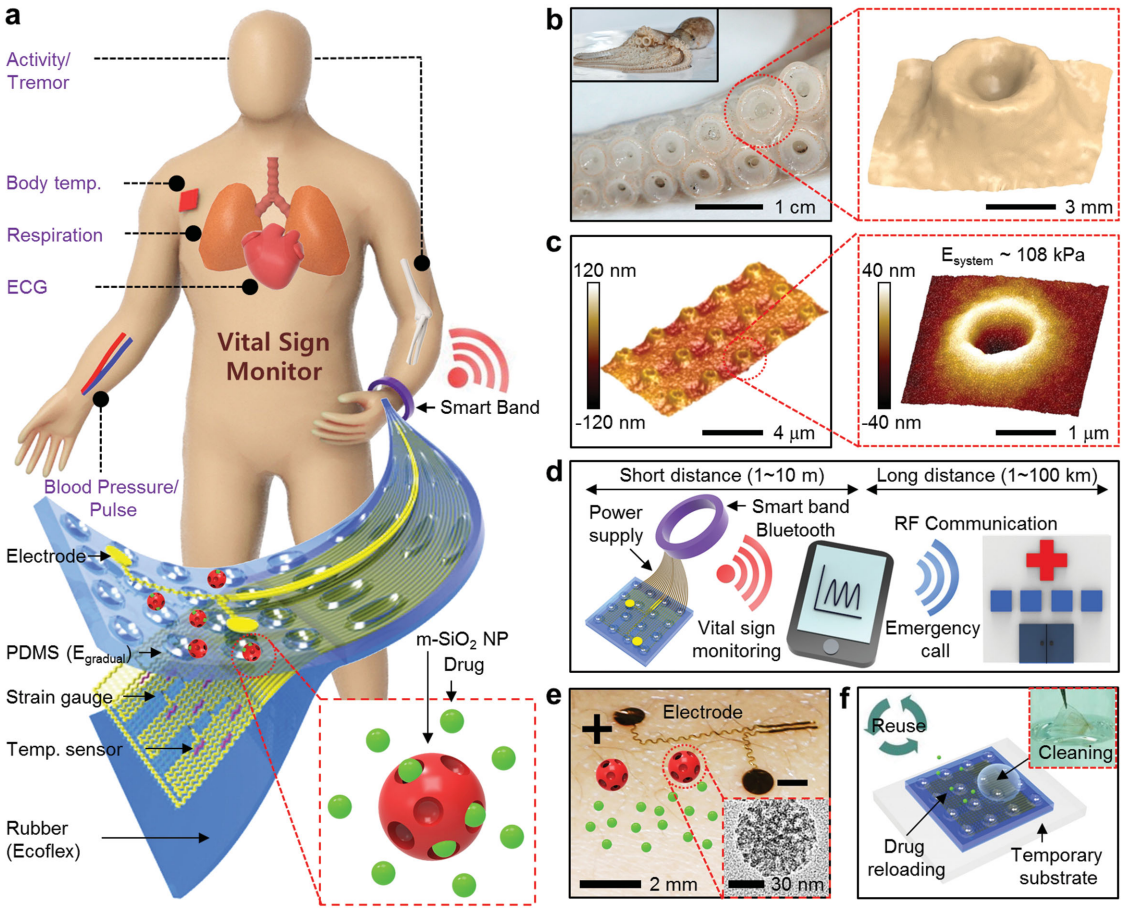

Figure 1. Overview of the electronic patch with bioinspired dry adhesives. a) Schematic illustration of the multifunctional miniaturized suction cup (mSC) electronic patch. Vital signs are monitored by electrodes, strain gauges, and temperature sensors. Drugs loaded in the mesoporous silica nanoparticles are transdermally delivered by iontophoresis. The mSC structures are located at the interface between the patch and skin as dry adhesives. The smart band (connected to the mSC patch) provides wireless functionalities and a power source. b) Photograph of the cephalopod tentacle (left; inset shows the entire octopus) and 3D laser scanning image of magnified suction cup (right). c) 3D AFM image of mSC array (left) and magnified view (right). The dimension is submicrometer and system modulus is ≈108 kPa. d) Schematic illustration of the wireless communication system. Short distance wireless network (Bluetooth) and power supply units are included in the custom-made smart band. Vital signs are transferred to smart devices through Bluetooth and transmitted to remote healthcare centers through RF communication units. e) Control of transdermal drug delivery rates wirelessly via iontophoresis. f) The electronic patch is reused after cleaning (inset) and drug reloading.

reloaded periodically on the electronic patch (Figure 1f). This system offers a range of possibilities for mobile, point-of-care medical services.

The fabrication process for the low modulus electronic patch in combination with the aforementioned mSC structures is described in Figure S4b (Supporting Information). First, the stretchable electronics (Figure S1, Supporting Information) are transferred onto ultrathin rubber (≈14 μm and ≈39 kPa) coated on the poly(vinylalcohol) (PVA) film. The hard-poly(urethane acrylate) (h-PUA) mold with intaglio mSC patterns with super-hydrophobic coating is separately prepared (Figure S4a, Supporting Information). The mold is sequentially spin-casted with diluted polydimethylsiloxane (PDMS) layers, whose modulus is gradually altered from ≈1.6 MPa to ≈500 kPa (Figure S5a–d, Supporting Information). The relatively high modulus (≈1.6 MPa) layer helps to form mSC structures, while the low modulus (≈500 kPa) layer provides a soft interfacial layer.[26] The thickness of coated PDMS layers (≈4 μm) is much thinner than the rest of the system (≈45 μm), thereby allowing the electronic patch with mSC arrays to achieve the ultralow system modulus (≈108 kPa), which is smaller than the modulus of epidermis (≈150 kPa), as shown in Figure S5 (Supporting Information). These fabrication steps are completed upon full cure and removal from the mold. Dissolution of the temporary PVA film finally allows lamination of the electronic patch on skin (Figure S2, Supporting Information).

Figure 2a shows scanning electron microscope (SEM) images of the cephalopod-inspired mSC (top) and the gecko-inspired miniaturized pillar (m-pillar; bottom) structures. Inset shows the top view of mSC structures. These two bioinspired structures are used to evaluate the tackiness of dry adhesives. Although m-pillars enhance adhesion strength by increasing surface area, these structures require relatively high modulus materials to maintain their shape without leaning, bending or collapsing.[26] The system modulus of m-pillar structures (≈1.4 MPa; Figure S5e,f, Supporting Information) is thus

DOI: 10.1002/adhm.201500285

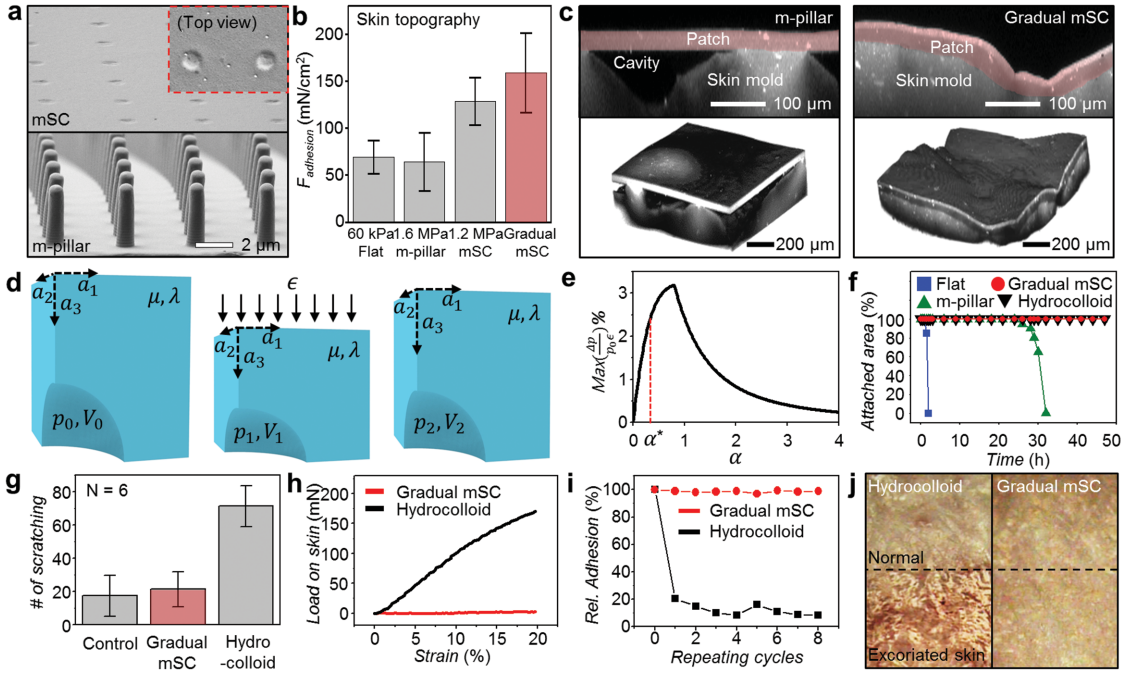

Figure 2. Bioinspired suction cups as comfortable dry adhesives. a) SEM images of the side view of mSCs (top; inset shows top-view of mSCs) and m-pillars (bottom). b) Change in adhesion force on the skin topology mold with different surface-structured patches (flat, m-pillars, and mSCs with different moduli). c) Confocal microscope images (cross-section and 3D view) at the vicinity of the contacting interface between structured patch and skin mold (left: m-pillar and right: gradual mSC). d) Spheroidal void embedded in the infinite body with Lame constants (μ, λ) and semiaxes (a_1, a_2, a_3) = (a, a, αa). The initial pressure and volume of the void (p_0, V_0) are changed to (p_1, V_1) when compressive strain ε is applied. After removing the load, the void would partially recover its shape to (p_2, V_2). e) The max ($\Delta p/p_0\varepsilon$) versus α. The α^* is computed to be 0.32 with dimension of mSCs (a_1 = 500 nm and a_3 = 160 nm). f) Durability tests of mSC patches on the back of mice in comparisons to flat, m-pillar, and commercial hydrocolloid patch. g) Scratching behavior test compared with hydrocolloid patch. h) Load on patch-attached skin when extra strain is applied. i) Change in the adhesion strength during recycling of mSC and hydrocolloid patch on the skin. j) Skin morphologies after three times of delaminating hydrocolloid patch (left) and mSC patch (right).

higher than that of the epidermis. In contrast, the mSCs with low aspect ratio (≈150 nm height and ≈950 nm diameter) can be readily fabricated with ultralow system modulus (≈108 kPa) and exhibit greater tackiness (Figure 2b) by a factor of ≈ 3 relative to m-pillars. Increased adhesion force comes from the conformally contacted skin-interface and suction effect of mSC structures. Confocal microscope images provide more information about enhanced adhesion forces and conformal contacts of mSCs over m-pillars on highly variable skin morphologies (Figure 2c).

The mechanics underlying enhanced adhesion of mSCs are analyzed theoretically by finite element modeling (FEM) (Supporting Information). Assuming that the mSCs are compressed against a frictionless surface, due to symmetry, a 2D array of mSCs on the surface of half space is equivalent to a 2D array of spheroids in an infinite body, where the Eshelby's inhomogeneity solution applies.[27] Due to this symmetry of the structure as well as loading conditions, the Eshelby's solution can be applied to the current system. As the stress field in Eshelby's problem decays with distance cubed, i.e., proportional to $1/r^3$, an mSC structure with radius of 500 nm, spacing of 4 mm, and patch thickness of 47 mm justifies negligible neighboring effects and the half space assumption. Therefore, the 2D array of spheroids can be simplified into a single spheroid model with an eighth of it depicted in Figure 2d, with the semiaxes of the spheroid being (a_1, a_2, a_3) = (a, a, αa). The initial pressure and volume of the mSC are given by p_0 and V_0, where p_0 denotes atmospheric pressure. Applying a compressive strain of ε on top of the patch will squeeze some air out of the mSCs, giving rise to new volume V_1, while pressure remains the same, i.e., $p_1 = p_0$. When ε is removed, assuming no air can come back to the mSC, the mSC volume will partially recover and the final pressure and volume becomes p_2 and V_2. Since $V_2 > V_1$, we expect $p_2 < p_0$, assuming the amount of gas in the mSC remains the same. Therefore, removal of ε effectively creates a negative pressure of $\Delta p = p_0 - p_2$ inside the mSC, and a resulting suction force.

To analytically solve nondimensionalized $\Delta p/(p_0\varepsilon)$ as a function of a, b, and n, where $a = a_3/a_1$, $b = p_0/m$, and m and n represent the shear modulus and Poisson's ratio of the matrix, respectively, we implement the following strategy (see Supporting Information Appendix for details). First, we use Eshelby's inhomogeneity solution to analytically derive $V_1(V_0, \varepsilon)$. Applying negative pressure Δp to a relaxed mSC allows calculation of the final volume $V_2(V_0, \Delta p)$. The ideal gas equation $p_0V_1(V_0,\varepsilon) = p_2V_2(V_0, p_0-p_2)$ becomes an equation with just one unknown variable, p_2, which is analytically solvable. Since Eshelby's solution is only valid for small deformation, we have implemented the following constraints on our solution: $0 \le \varepsilon \le 5\%$ and $0 \le (V_0 - V_1)/V_0 \le 10\%$. Practically, it is also required that $0 \le p_2 \le p_0$. The analytical solution under these constraints is plotted in Figure 2e, with $b = 2.8$ (p_0 = 101 kPa, m = 36 kPa) and n = 0.499 fixed. As shown in Figure 2e, the

maximum allowable $\Delta p/p_0$ first increases and then decreases with α, suggesting an optimum α can be found with the given constraints. Experimentally, α^* is computed to be 0.32 with a_1 = 500 nm and a_3 = 160 nm, which is highlighted in Figure 2e. In addition to mSC shape, material properties including m and n can also affect max($\Delta p/p_0$).

Wearable patches often cause time-dependent irritation and discomfort.[28] To quantify the effects of wear on the skin, we designed animal model studies to assess behaviors in response to patch wear. We monitored mice fitted with these wearable patches and used a video camera to monitor their behaviors in cages (Figure S6a,b, Supporting Information). A detailed description of the experiment to observe animal behavior is included in Supporting Information. Briefly, electronic patches are laminated on the back skin of each mouse. We recorded the number of scratches over 3 h to assess the degree of irritation. To evaluate long-term wearability, we compared the durability of mSCs patches relative to m-pillar/flat patches and commercial hydrocolloid patches by affixing patches to the lower back surface of mice. The mSCs and hydrocolloid patches firmly adhered on mice skin for over 2 d, whereas the m-pillar and flat patches delaminated in 2 and 30 h, respectively, due to weaker adhesion and mechanical interaction with skin (Figure 2f).

Therefore we excluded m-pillar and flat patches then compared the degree of the comfort of the mSC patches with commercial hydrocolloid patches that show good adhesion by relying on chemical adhesives. The number of scratches recorded with mSC patches is similar to the control (mice with bare back), while the number of scratches counted with commercial hydrocolloid patches is four times higher (Figure 2g). The difference in shear forces applied to the skin (Figure 2h) explains scratching tendencies. The higher stiffness of the commercial hydrocolloid patches induces the higher loads/strains on the skin, which in turn give rise to high skin discomfort, while vice versa in the mSC patches. This behavior analysis agrees with FEM simulations (Figure S6e,f, Supporting Information). See Figure S6c-l (Supporting Information) for more details about the relation between the patch stiffness and scratch count.

Another important aspect of electronic patches is the reusability.[29] The mSC patch maintains its adhesion strength for ≈8 cycles of reuse, whereas the hydrocolloid patch loses its adhesion force significantly after the first use, causing detachment from the skin (Figure 2i) and thereby difficulty to reuse electronics. This reusing of smart medical skin enables refreshing the skin surface in the long-term use. Figure 2j shows skin conditions following three attachment/detachment cycles over the course of 1 d (dry adhesives in mSC patch and chemical adhesives in hydrocolloid patch). The top half of the frame shows bare skin without patch while the bottom half shows a skin segment under the patch. Black dotted lines show the border between two segments. The skin laminated with a hydrocolloid patch (left) undergoes some amount of abrasion and scarring that is visually observed, while skin in contact with the mSC patch (right) remains intact. Fluffs are also peeled off by the hydrocolloid patch in the regions of skin with rashes and scarring (compare images of Figure S7a,b, Supporting Information). Moreover, skin segments underneath the hydrocolloid patches exhibited an inflammatory response. This is evident in the Hematoxylin and eosin (H&E) histological stains, which show the presence of macrophages and other inflammatory cells near the dermis for the hydrocolloid patch (Figure S7c, Supporting Information). The mSC did not exhibit any inflammatory responses and biocompatibility was confirmed in the human wearability experiment, in which the mSC patch was laminated on human arms for 4 d (Figure S7d–f, Supporting Information).

Conformal integration of ultrathin electronic sensors onboard mSC smart skin establishes a tight skin-interfaced platform for vital sign monitoring with high sensitivity. For example, strain gauges (Figure S8a,b, Supporting Information) integrated on mSC patch have high sensitivity to precisely detect an arterial pulse wave from the radial artery of a healthy subject (Figure S9a, Supporting Information) without the external pressure (**Figure 3**a, top). In contrast, strain gauges on the m-pillar and hydrocolloid patches cannot detect slight changes of small arterial pulse without external pressure (Figure 3a, middle and bottom).[26,30] Arterial pulse signals noninvasively measured by the mSC electronic patch are sufficiently accurate to obtain clinically important information on cardiovascular aging, i.e., to distinguish the dicrotic notch (a tiny dig between systolic and diastolic phase in the arterial pressure waveform) and the slope of the pulse (Figure 3b). With aging or the increase of arterial stiffness, the dicrotic notch in the arterial waveform becomes less pronounced and the slope is steeper.[31] Figure 3b shows a representative example of a mSC electronics-measured arterial waveform with distinct dicrotic notch and less steep slope in a young subject (a 23-year-old male) when compared with that with less prominent notch and steep slope in an old subject (a 50-year-old male). The peak values of arterial pulse waves obtained from mSCs during daily activity of resting, eating, and exercise (Figure 3c) are linearly correlated with systolic blood pressure measured by a commercial blood pressure gauge at the identical time, suggesting the potential function as a blood pressure monitor (inset of Figure 3c).

Moreover, the real-time ECGs are simultaneously measured with integrated electrodes, as shown in Figure 3d (detailed numbers are indicated at the top). Effective adhesiveness of mSCs to the skin enables to monitor the pulse and ECG consistently without drift or distortion during exercise as well as resting state (Figure 3d). Since ultraconformal lamination of mSC electronics on the epidermis remarkably reduces far-field noises, subtle change of electrical signals originating from the heart can be detected with high sensitivity, allowing distinct discrimination of a P-wave with small amplitude of ≈2.5 mV, a QRS complex, and a T-wave in ECGs (Figure 3e). It helps to differentiate various cardiac arrhythmic diseases, most of which are diagnosed from accurate detection of a P-QRS-T-wave.

The measurement of chest wall movement provides respiratory information under various conditions, as shown in Figure 3f. The skin temperature changes indoor (warm) and outdoor (cold) are also monitored using temperature sensors on human arms (Figure S8c,d, Supporting Information), which are exactly matched with commercial IR camera measurement (Figure 3g). Body temperature can be measured by positioning mSC patch on the axillary area, possibly providing important medical information on fever or hypothermia manifested in various diseases. In addition to vital signs, physical activities

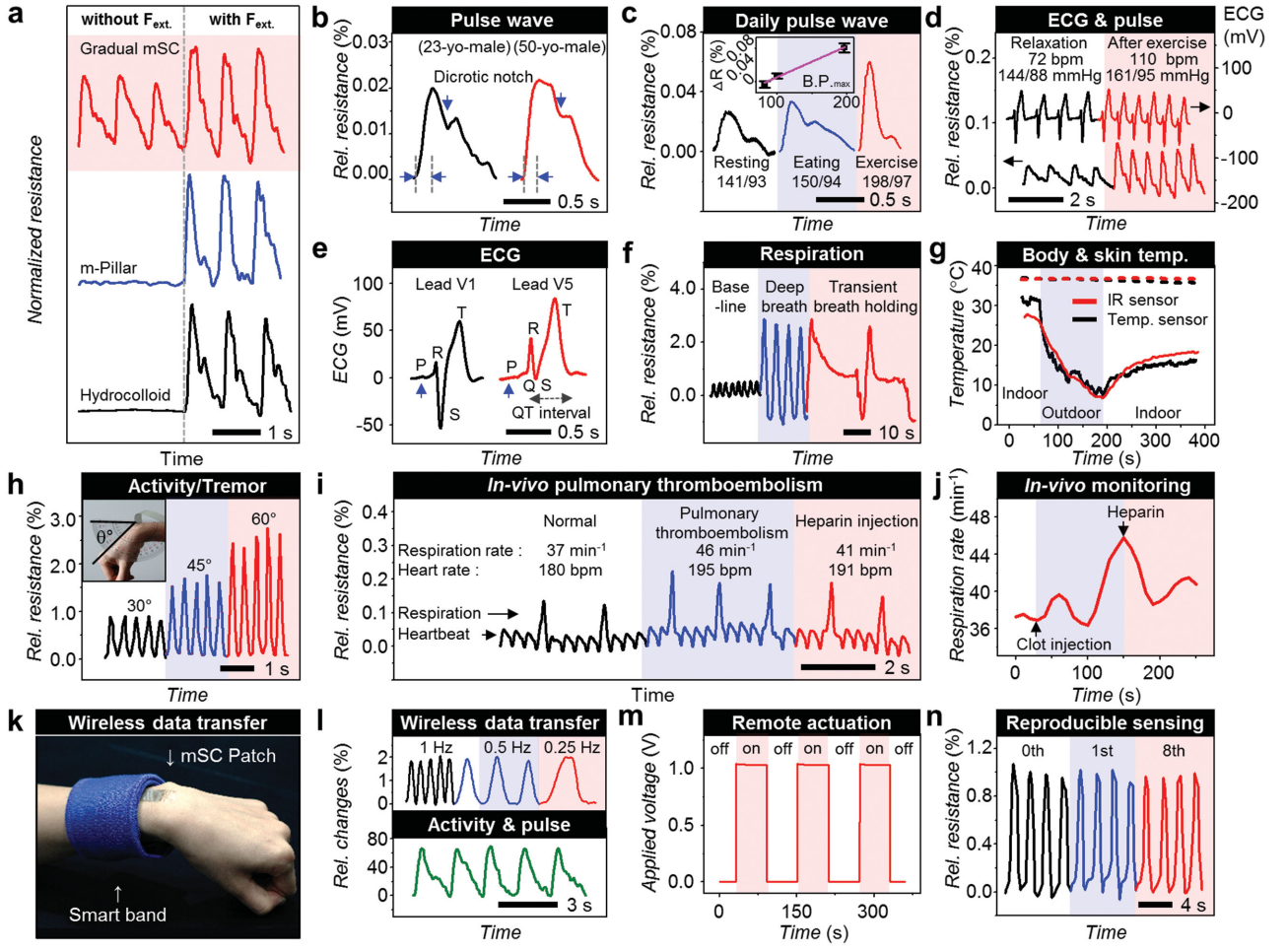

Figure 3. Measurement of vital signs, detection of acute medical conditions, and wireless communications. a) Pulse waves measured on the radial artery with/without external pressure. Only mSC patch can record pulse waves without pressurization. b) Comparison of an arterial pulse waveform between the different age groups (23-year-old male and 50-year-old male). c) Changes of arterial pulse waves during daily activity. The peak intensity correlates linearly with the systolic blood pressure (inset). d) Variation in vital signs due to exercises (top: ECG signals from electrodes, bottom: pulse signals from Si strain gauges). e) Surface ECGs recorded on the chest. The electrical waveforms of a P-QRS-T complex are reproduced from the V1 and V5 sites, respectively. f) Change in relative resistance at various respiration patterns including baseline, deep breath, and transient breath holding. g) Variance in the body (dashed line) and skin (line) temperature under indoors and outdoors. h) Movement signals as changing angles of joint motion. Inset shows the image of measuring strain. i,j) Variation in respiration and heartbeats in a mouse model of acute pulmonary thromboembolism induced by intravenous injection of massive blood clots and treated with heparin (i). Change in respiration rate at whole time range (j). k) Image of wireless communication settings. The mSCs patch is connected with the smart band which involves the Bluetooth unit and the battery. l) Tremor and pulse data wirelessly received from the Bluetooth system. m) Remotely controlled voltage to turn iontophoresis on/off for the transdermal drug delivery. n) Tested strain gauge functionality after eight times recycling.

are quantified by characterizing the joint movement frequency with angular changes (Figure 3h and Figure S9b,c, Supporting Information). With the help of mSC structures, the smart skin achieves tight coupling on the skin even under dynamic motions. Tremor caused by physiologic or pathophysiologic conditions including Parkinson's disease can also be monitored (Figure S9d, Supporting Information).

Continuous monitoring of vital sign changes with mSCs can help detect acute medical conditions,[32] thereby facilitating medical assists through wireless connections to emergency clinical service providers. In animal experimental models (Balb/c nude mouse) of acute medical conditions including hypothermia, hypertensive emergency, and massive pulmonary thromboembolism, vital signs are monitored in vivo with skin-coupled mSC electronic patches. In the massive pulmonary thromboembolism models, sudden elevation of respiratory and heart rates are alarmed and recovered by immediate intravenous infusion of 50 μg heparin (Figure 3i,j). In the animal experimental models of acute hypothermia induced by ethanol tap on the body, body temperature, heart rate, and respiratory rate are monitored by its simultaneous multirecording system. The early detection of slow heart rate and depressed respiration with low body temperature following hypothermia facilitates the rapid treatment such as warming (Figure S10a,b, Supporting Information). In the norepinephrine-induced hypertensive models, heart rates are abruptly elevated and stabilized with the subsequent administration of 100 μg propranolol (Figure S10c,d, Supporting Information).

Figure 3k–m shows wireless data transmission and controlled drug release through the Bluetooth unit of the custom-made smart band (Figure S3, Supporting Information) in conjunction with commercial devices, such as the smartphone. The electronic patch contains essential components, such as sensors, actuators, and drug-loaded nanoparticles, while all other expensive wireless, power storage, and controller units are incorporated in the smart band. This strategy allows conformal integration of the electronic patch on skin by decreasing the thickness and stiffness of the patch. Moreover, the cost and size of the patch can be reduced.

Figure 3k shows the multifunctional electronic patch connected to the smart band. This system transmits recorded data (vital signs and activities/tremors) wirelessly to external devices in real time (Figure 3l and Movie S1, Supporting Information). While short-range communications occur through the Bluetooth unit in the custom-made smart band, long-range communications are achieved with a commercial smartphone (Figure 1d and Figure S3b, Supporting Information). Therefore, biosignals including vital signs, physical activity, and tremor can be transmitted wirelessly. In emergency situations, the custom-made Labview software installed in the controller unit determines the states and signals an alarm to remote healthcare units (Movie S1, Supporting Information). Moreover, Figure 3m and Movie S2 (Supporting Information) show the concept of telemedicine, the wireless control of transdermal drug delivery via integrated iontophoresis electrodes. Using an Android application installed in a smartphone, remote medical providers can control the drug delivery rate.

The multifunctional mSC electronic patch allows highly sensitive monitoring of vital signs for long time, detection of acute medical conditions, and wireless communications from/to external devices. These functionalities are useful in preventive medicine and point-of-care clinical applications. System design strategies separating electronic patches from the smart band together with the patch reuse (Figure 1f and Figure S11, Supporting Information) reduce the financial burden of patients. Even after 8 cycles of reuse, the electronic patch shows stable/reproducible sensing signals (Figure 3n).

We integrate the iontophoresis electrodes in the mSC patch to control transdermal drug delivery rate.[33] This integration is the first demonstration of iontophoretic drug delivery applied to the ultrathin wearable electronic patch. The m-SiO_2 nanoparticles (**Figure 4**a) were utilized as drug delivery vehicles, which prevent oxidation, denaturation, and unstimulated diffusion of drugs.[34] Nanopores inside m-SiO_2 nanoparticles provide large surface area for drug adsorption and loading.[35] The insets of Figure 4a show the confocal images of fluorescent drug (doxorubicin; red, center) loaded on m-SiO_2 carriers (green, left). The right inset shows the combined image (yellow). The system incorporates the iontophoresis approach for drug delivery, in which medications are smeared deeply under the skin by the charge repulsion between electrodes and drugs. Iontophoresis has advantages over the thermal diffusion in preventing low-temperature-burn-injury and/or thermal denaturation of drugs.

The amount of drug delivery is controlled by stimulus number of iontophoresis and thermal diffusion; 1 min

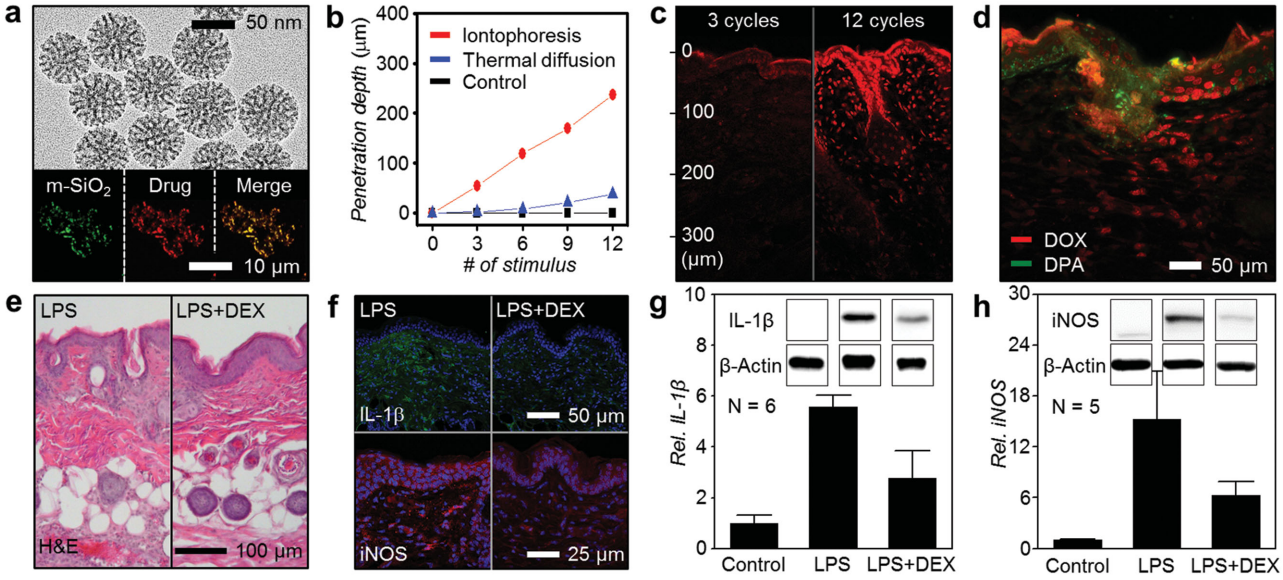

Figure 4. Controlled transdermal drug delivery via iontophoresis. a) TEM image of drug-loaded mesoporous silica nanoparticles (m-SiO_2). The inset shows unified confocal image of m-SiO_2 (green) and fluorescent drug (doxorubicin, red). b) Stimulus number versus drug diffusion length into the mouse skin with different actuators (black: none, blue: thermal actuator, and red: iontophoresis electrode). c) Cross-sectional fluorescence images for the drug (doxorubicin) diffusion into the mouse skin with different stimuli of iontophoresis; 3 cycles (left) and 12 cycles (right). d) The cross-sectional confocal fluorescence image which demonstrates the sequentially diffused two different dyes into the mouse skin (red: doxorubicin, green: 9,10-diphenylanthracene). e) The H&E stain histology of the LPS-injected mouse skins before (left) and after (right) DEX treatment. f) Immunohistochemistry of interleukin-1β (IL-1β, green) and iNOS, red before (left) and after (right) DEX treatment. Nuclei are marked with 4′,6-diamidino-2-phenylindole (DAPI, blue). g,h) Western blot immunoassay of IL-1β (g) and iNOS (h). The insets show the representative band intensity due in the expressed inflammatory mediators.

Adv. Healthcare Mater. **2015**,
DOI: 10.1002/adhm.201500285

stimulus and 3 min break was defined as one cycle of external stimulus. As shown in Figure 4b, diffusion depth of the doxorubicin into Balb/c mouse skin is proportional to the number of applied stimulus. The drug penetration depth by iontophoresis is ≈200 μm, which is the depth of epidermis and upper dermis, within 12 stimuli. The depth by thermal diffusion (at ≈37 °C; ≈12 °C higher than the normal body temperature of mouse) is much shallower (≈35 μm). Drug diffusion without external stimuli is negligible during that time period. The diffusion depth of ≈30 μm was observed by the natural diffusion after 48 h attachment of the patch. The confocal microscope images (red: doxorubicin) show the difference of drug diffusion depths into mouse skin at different cycles of iontophoresis (Figure 4c left and right for 3 and 12 cycles, respectively).

Another benefit of the mSC dry adhesives is that pharmacological agents are easily reloaded by using temporary substrates and cleaning agents (Movie S3, Supporting Information). Figure S12 (Supporting Information) shows sequential confocal microscope images of the iontophoresis electrode after loading drug (red: doxorubicin), washing the electrode after use, and reloading different dye (green: 9,10-diphenylanthracene (DPA)), respectively. These two are sequentially delivered to the mouse skin by iontophoresis stimuli (Figure 4d). The stimulus number of doxorubicin was doubled over that of DPA and thereby doxorubicin diffusion depth is twice of DPA.

Therapeutic effects using the mSC electronic patch are demonstrated by in vivo animal experiments. The lipopolysaccharide (LPS) and bacterial endotoxin initiates inflammatory responses, inducing reactive oxygen species and various inflammatory cytokines. Drug-loaded mSC patch was laminated on the LPS-injected mouse skin and 12 cycles of iontophoresis were applied for anti-inflammatory agent (dexamethasone) diffusion. To verify the therapeutic effect, histopathological (H&E staining; Figure 4e), immunofluorescence (Figure 4f), and western blot (Figure 4g,h) analysis were employed. As shown in Figure 4f, the immunofluorescence stainings of skin tissues show that the treatment of dexamethasone (DEX) significantly suppresses expressions of inflammatory mediators, interleukin-1β (IL-1β, green) and inducible nitric oxide synthase (iNOS, red), compared with LPS-injected bare skin. The western blot data also demonstrates the reduced expression levels of IL-1β (Figure 4g) and iNOS (Figure 4h) by the DEX treatment, confirming transdermal penetration through iontophoresis.

In conclusion, we developed cephalopod-inspired dry adhesives integrated with physiological sensors, drug-delivery actuators, and therapeutic nanoparticles in an ultrathin and stretchable format. The biomimetic structures enhance adhesion and comfort, limit tissue damage and inflammations, and allow sensitive biometric measurement and transdermal drug delivery by virtue of tight skin coupling. Wireless connection of the electronic patch through a Bluetooth-enabled band allows data transmission in real time and provides a path for remote diagnostics and treatments, forwards bioinspired "smart medical skin".

Experimental Section

Detailed information for the Experimental Section is in the Supporting Information.

Supporting Information

Supporting Information is available from the Wiley Online Library or from the author.

Acknowledgements

M.K.C., O.K.P, and C.C. contributed equally to this work. This work was supported by IBS-R006-D1. This work was also supported by a grant from the Basic Science Research Program of the National Research Foundation of Korea (NRF), funded by the Ministry of Science, ICT, and Future Planning (Grant No. 2012R1A1A1004925). In addition, this work was supported by the Seoul National University Research Grant. N.L. acknowledges the US NSF CMMI award under Grant No. 1301335.

Received: April 17, 2015
Revised: April 29, 2015
Published online:

[1] K. Autumn, Y. A. Liang, S. T. Hsieh, W. Zesch, W. P. Chan, T. W. Kenny, R. Fearing, R. J. Full, *Nature* **2000**, *405*, 681.
[2] N. Huebsch, D. J. Mooney, *Nature* **2009**, *462*, 426.
[3] A. Mahdavi, L. Ferreira, C. Sundback, J. W. Nichol, E. P. Chan, D. J. D. Carter, C. J. Bettinger, S. Patanavanich, L. Chignozha, E. Ben-Joseph, A. Galakatos, H. Pryor, I. Pomerantseva, P. T. Masiakos, W. Faquin, A. Zumbuehl, S. Hong, J. Borenstein, J. Vacanti, R. Langer, J. M. Karp, *Proc. Natl. Acad. Sci. U.S.A.* **2008**, *105*, 2307.
[4] J.-Y. Sun, X. Zhao, W. R. K. Illeperuma, O. Chaudhuri, K. H. Oh, D. J. Mooney, J. J. Vlassak, Z. Suo, *Nature* **2012**, *489*, 133.
[5] S. Y. Yang, E. D. O'Cearbhaill, G. C. Sisk, K. M. Park, W. K. Cho, M. Villiger, B. E. Bouma, B. Pomahac, J. M. Karp, *Nat. Commun.* **2013**, *4*, 1702.
[6] A. K. Geim, S. V. Dubonos, I. V. Grigorieva, K. S. Novoselov, A. A. Zhukov, S. Y. Shapoval, *Nat. Mater.* **2003**, *2*, 461.
[7] T.-i. Kim, H. E. Jeong, K. Y. Suh, H. H. Lee, *Adv. Mater.* **2009**, *21*, 2276.
[8] H. E. Jeong, J.-K. Lee, H. N. Kim, S. H. Moon, K. Y. Suh, *Proc. Natl. Acad. Sci. USA* **2009**, *106*, 5644.
[9] H. Yoon, H. E. Jeong, T.-i. Kim, T. J. Kang, D. Tahk, K. Char, K. Y. Suh, *Nano Today* **2009**, *4*, 385.
[10] H. Lee, B. P. Lee, P. B. Messersmith, *Nature* **2007**, *448*, 338.
[11] D.-H. Kim, J. Viventi, J. J. Amsden, J. Xiao, L. Vigeland, Y.-S. Kim, J. A. Blanco, B. Panilaitis, E. S. Frechette, D. Contreras, D. L. Kaplan, F. G. Omenetto, Y. G. Huang, K.-C. Hwang, M. R. Zakin, B. Litt, J. A. Rogers, *Nat. Mater.* **2010**, *9*, 511.
[12] M. Kaltenbrunner, T. Sekitani, J. Reeder, T. Yokota, K. Kuribara, T. Tokuhara, M. Drack, R. Schwodiauer, I. Graz, S. Bauer-Gogonea, S. Bauer, T. Someya, *Nature* **2013**, *499*, 458.
[13] D.-H. Kim, N. Lu, R. Ma, Y.-S. Kim, R.-H. Kim, S. Wang, J. Wu, S. M. Won, H. Tao, A. Islam, K. J. Yu, T.-i. Kim, R. Chowdhury, M. Ying, L. Xu, M. Li, H.-J. Chung, H. Keum, M. McCormick, P. Liu, Y.-W. Zhang, F. G. Omenetto, Y. Huang, T. Coleman, J. A. Rogers, *Science* **2011**, *333*, 838.
[14] S. Lee, Y. Inoue, D. Kim, A. Reuveny, K. Kuribara, T. Yokota, J. Reeder, M. Sekino, T. Sekitani, Y. Abe, T. Someya, *Nat. Commun.* **2014**, *5*, 5898.
[15] C. Keplinger, J.-Y. Sun, C. C. Foo, P. Rothemund, G. M. Whitesides, Z. Suo, *Science* **2013**, *341*, 984.
[16] J. Kim, M. Lee, H. J. Shim, R. Ghaffari, H. R. Cho, D. Son, Y. H. Jung, M. Soh, C. Choi, S. Jung, K. Chu, D. Jeon, S.-T. Lee, J. H. Kim, S. H. Choi, T. Hyeon, D.-H. Kim, *Nat. Commun.* **2014**, *5*, 5747.

[17] S. Jung, J. H. Kim, J. Kim, S. Choi, J. Lee, I. Park, T. Hyeon, D.-H. Kim, *Adv. Mater.* **2014**, *26*, 4825.
[18] S. Jung, J. Lee, T. Hyeon, M. Lee, D.-H. Kim, *Adv. Mater.* **2014**, *26*, 6329.
[19] S. Lim, D. Son, J. Kim, Y. B. Lee, J.-K. Song, S. Choi, D. J. Lee, J. H. Kim, M. Lee, T. Hyeon, D.-H. Kim, *Adv. Funct. Mater.* **2015**, *25*, 375.
[20] M. Park, K. Do, J. Kim, D. Son, J. H. Koo, J. Park, J.-K. Song, J. H. Kim, M. Lee, T. Hyeon, D.-H. Kim, *Adv. Healthcare Mater.* **2015**, DOI: 10.1002/adhm.201500097.
[21] K. Takei, T. Takahashi, J. C. Ho, H. Ko, A. G. Gillies, P. W. Leu, R. S. Fearing, A. Javey, *Nat. Mater.* **2010**, *9*, 821.
[22] D. J. Lipomi, M. Vosgueritchian, B. C. K. Tee, S. L. Hellstrom, J. A. Lee, C. H. Fox, Z. Bao, *Nat. Nanotechnol.* **2011**, *6*, 788.
[23] D. Son, J. Lee, S. Qiao, R. Ghaffari, J. Kim, J. E. Lee, C. Song, S. J. Kim, D. J. Lee, S. W. Jun, S. Yang, M. Park, J. Shin, K. Do, M. Lee, K. Kang, C. S. Hwang, N. Lu, T. Hyeon, D.-H. Kim, *Nat. Nanotechnol.* **2014**, *9*, 397.
[24] W.-Y. Chang, Y. Wu, Y.-C. Chung, *Nano Lett.* **2014**, *14*, 1546.
[25] A. del Campo, C. Greiner, I. Alverez, E. Arzt, *Adv. Mater.* **2007**, *19*, 1973.
[26] W. G. Bae, D. Kim, M. K. Kwak, L. Ha, S. M. Kang, K. Y. Suh, *Adv. Healthcare Mater.* **2013**, *2*, 109.
[27] J. D. Eshelby, *Proc. R. Soc. A* **1957**, *241*, 376.
[28] M. K. Kwak, H.-E. Jeong, K. Y. Suh, *Adv. Mater.* **2011**, *23*, 3949.
[29] K.-I. Jang, S. Y. Han, S. Xu, K. E. Mathewson, Y. Zhang, J.-W. Jeong, G.-T. Kim, R. C. Webb, J. W. Lee, T. J. Dawidczyk, R. H. Kim, Y. M. Song, W.-H. Yeo, S. Kim, H. Cheng, S. I. Rhee, J. Chung, B. Kim, H. U. Chung, D. Lee, Y. Yang, M. Cho, J. G. Gaspar, R. Carbonari, M. Fabiani, G. Gratton, Y. Huang, J. A. Rogers, *Nat. Commun.* **2014**, *5*, 4779.
[30] L. Y. Chen, B. C. K. Tee, A. L. Chortos, G. Schwartz, V. Tse, D. J. Lipomi, H.-S. P. Wong, M. V. McConnell, Z. Bao, *Nat. Commun.* **2014**, *5*, 5028.
[31] S. Laurent, J. Cockcroft, L. Van Bortel, P. Boutouyrie, C. Giannattasio, D. Hayoz, B. Pannier, C. Vlachopoulos, I. Wilkinson, H. Struijker-Boudier, *Eur. Heart. J.* **2006**, *27*, 2588.
[32] C. Pang, J. H. Koo, A. Nguyen, J. M. Caves, M.-G. Kim, A. Chortos, K. Kim, P. J. Wang, J. B.-H. Tok, Z. Bao, *Adv. Mater.* **2015**, *27*, 634.
[33] M. R. Prausnitz, R. Langer, *Nat. Biotechnol.* **2008**, *26*, 1261.
[34] J. E. Lee, N. Lee, T. Kim, J. Kim, T. Hyeon, *Acc. Chem. Res.* **2011**, *44*, 893.
[35] Y. Gao, Y. Chen, X. Ji, X. He, Q. Yin, Z. Zhang, J. Shi, Y. Li, *ACS Nano* **2011**, *5*, 9788.

ADVANCED HEALTHCARE MATERIALS

Supporting Information

for *Adv. Healthcare Mater.,* DOI: 10.1002/adhm.201500285

Cephalopod-Inspired Miniaturized Suction Cups for Smart Medical Skin

*Moon Kee Choi, Ok Kyu Park, Changsoon Choi, Shutao Qiao, Roozbeh Ghaffari, Jaemin Kim, Dong Jun Lee, Myungbin Kim, Wonji Hyun, Seok Joo Kim, Hye Jin Hwang, Seung-Hae Kwon, Taeghwan Hyeon, Nanshu Lu, and Dae-Hyeong Kim**

Supporting Information

Cephalopod-inspired Miniaturized Suction Cups for Smart Medical Skin

*Moon Kee Choi[†], Ok Kyu Park[†], Changsoon Choi[†], Shutao Qiao, Roozbeh Ghaffari, Jaemin Kim, Dong Jun Lee, Myungbin Kim, Wonji Hyun, Seok Joo Kim, Hye Jin Hwang, Seung-Hae Kwon, Taeghwan Hyeon, Nanshu Lu, Dae-Hyeong Kim**

[†]M. K. Choi, O. K. Park and C. Choi contributed equally to this work.

Keywords: biomimetic; dry adhesive; physiological sensing; drug delivery

1. Supporting Text

1.1. Model for Negative Pressure in Compressed mSCs

As discussed in the main text, a 2D array of miniaturized suction cups (mSCs) of half space can be simplified as a single spheroidal void in an infinite body. When arbitrary remote loading ϵ^0 is applied (Figure 2D, middle), assuming void pressure remains unchanged, the volume change of the void is going to be,

$$V_1 - V_0 = \epsilon_{kk} V_0 = [\epsilon^0 - S(S-I)^{-1}\epsilon^0]_{kk} V_0 \quad (1)$$

where I is the 4th-order identical tensor and S is the 4th-order Eshelby tensor[S1] which are determined by the geometry of the void and the Poisson's ratio of the matrix material. After remote loading is removed, the final pressure and volume becomes p_2 and V_2 as the void volume can be partially recovered (Figure 2D, right). Using the superposition illustrated in Figure S13a, the strain field in the void can be obtained and expressed as follows:

$$\epsilon_{ij} = {\epsilon_{ij}}^1 + {\epsilon_{ij}}^2$$

$$= \frac{p_0 - p_2}{2\mu + 3\lambda}\delta_{ij} - [I - S(S-I)^{-1}]_{ijkl}\frac{p_0 - p_2}{2\mu + 3\lambda}\delta_{kl}$$

$$= [S(S-I)^{-1}]_{ijkk}\frac{p_0 - p_2}{2\mu + 3\lambda} \quad (2)$$

where μ and λ are Lamé constants of the matrix material. Thus the volume change after the remote loading removed is written as

$$V_2 - V_0 = [S(S-I)^{-1}]_{iikk}\frac{p_0 - p_2}{2\mu + 3\lambda} V_0 \quad (3)$$

When uniaxial compressive strain, $\epsilon_{11} = \epsilon_{22} = -\nu\epsilon_{33} = \nu\epsilon$ ($\epsilon > 0$), is applied remotely to

the infinite body with a spheroidal void which has three semi axes (a_1, a_2, a_3) = $(a, a, \alpha a)$, the negative pressure in the void can be found by combining equation (1), (3) and $p_0V_1 = p_2V_2$ and is written as

$$\frac{\Delta p}{p_0} = \frac{p_0 - p_2}{p_0} \approx \frac{C_1}{1+3\beta C_2/4}\epsilon \qquad (4)$$

where

$$C_1 = \frac{(1-\nu)[4-5g+4\nu(1-2g)+2(1-2g)(1-2\nu)\alpha^2]}{2[g+2\alpha^2-4\alpha^2 g-(1-\alpha^2)(1+\nu)g^2]} \quad (5)$$

$$C_2 = \frac{6(1-2\nu)(1-\alpha^2)g^2-4\nu(1-3g)(1-\alpha^2)+4+2\alpha^2-9g}{3[g+2\alpha^2-4g\alpha^2-(1-\alpha^2)(1+\nu)g^2]} \quad (6)$$

and

$$g = \begin{cases} \frac{\alpha}{(1-\alpha^2)^{3/2}}\left(\text{acos}(\alpha) - \alpha\sqrt{1-\alpha^2}\right) \text{ for } \alpha < 1 \\ \frac{\alpha}{(\alpha^2-1)^{3/2}}\left(\alpha\sqrt{\alpha^2-1} - \text{acosh}(\alpha)\right) \text{for } \alpha > 1 \end{cases} \qquad (7)$$

The FEM simulations (Figure S13 b and c) are also performed to validate the theoretical results given by equation (1) and (3). The infinite body is modeled as an axisymmetric bulk material (element type: CAX4R, Young's modulus: 108 kPa, Poisson's ratio: 0.499) under uniaxial compressive strain ϵ = 1% in the axial direction. Spheroidal voids with six different values of α (0.4, 0.5, 0.6, 0.7, 1, and 2) are modeled in FEM and comparisons between the numerical and the theoretical values are graphed in Figure S13 d and e. As we can see from Figure S13 d and e, the theoretical values matched the FEM results which have validated our derivation.

1.2. Animal behavior test (monitoring number of scratches)

In order to quantify the degree of discomfort after wearing patches, we performed the animal behavior test by using the mouse model. For the similarity with the human skin, nude mice (Balb/c nude mice) were used. We assumed a high degree of discomfort due to the wear of patches would lead to more scratching behavior.[S2,S3] Thus the count of scraping action in three different experimental sets (mouse of bare back, back with the mSC patch, back with the commercial hydrocolloid patch) can be a good factor for the quantification of the discomfort induced by different patches.

To visually observe animal behavior, we laminated patches on the back of mice and allowed the mice to swim in water for ~3 minutes. The purpose of the swimming is to remove residual PVA (water-soluble temporary supporting layer) and to confirm conformal mechanical coupling between the patch and the mouse skin. Each mouse was kept in its own cage to isolate each other. Scratching during experiments was monitored for ~3 hours across six mice. To minimize the influence of different time slots and individual differences between animals, behavior tests were carried out during the same time zone and the mice were experimented in turns. The interval of animal behavior tests spanned across ~1 week to ensure that the mice were stable. Scratching behavior in anatomical regions adjacent to the patch were included, while grooming actions were excluded.

The effect of patch stiffness on comfort was also estimated via similar animal behavior tests. Ultra-soft patches of different thicknesses (~30 μm, ~150 μm, and ~500 μm) were employed using the same experimental set-up and conditions with the aforementioned animal behavior test. The thinnest patches (~30 μm) exhibited the lowest scratching number, which implies highest comfort levels, whereas the thick one resulted in the opposite (Figure S6 c and d). These trends were analyzed by comparing the number of scratches with the

stiffness of each patch. Stiffer (thicker) patches tended to cause more strain on the skin and thereby more scratches/discomfort. FEM simulations (uniaxial strain for Figure S6 e-h and biaxial strain for Figure S6 i-l) corroborated with the experimental results, i.e. the ultrasoft mSC patch caused negligible irritation.

2. Supporting Methods

2.1. Fabrication of mSC molds

First, Si molds with the dot-shape trench array of ~500 nm radius and ~3 μm height are prepared by the deep reactive ion etching (Versaline, PLASMA THERM, USA) using the inductively coupled plasma. The surface of Si molds is treated with trichloro(1H,1H,2H,2H-perfluorooctyl)silane (FOTCS) self-assembled monolayer (SAM). Then the hard polyurethane acrylate (h-PUA; MINS 311 RM, Minuta Tech., Korea) is coated and photo-cured on it. Quick detachment of the h-PUA film after its uniform filling into deep trenches of the Si mold achieves the array of mountaintop-shaped h-PUA structures on the Si mold. The weak oxygen plasma etching of the h-PUA structures on the Si mold provides a circular groove near the border of Si trench, since Si is not etched while h-PUA is etched. This groove serves as a rim of mSCs. After FOTCS SAM treatment of the prepared h-PUA/Si mold, another layer of h-PUA is coated, cured, and detached. Then, the mSC mold made of h-PUA is obtained.

2.2. Device fabrication

The device fabrication begins with spin coating the precursor (~1 μm thick film) of polyimide (polyamic acid, Sigma Aldrich, USA) or benzocyclobutene (cyclotene 3022, Dow Chemical, USA) on a sacrificial layer (poly(methylmethacrylate) (PMMA A2, MicroChem, USA) or thermally deposited nickel layer). 100 nm thick Boron doped Si nano-membranes are prepared from the silicon-on-insulator wafer (SOITEC, France) and then transferred onto

prepared polymer films. Desired geometries of electronics are achieved by photolithography and dry etching processes. A lift-off process of Ti/Pt (5/40 nm) film is used for temperature sensors. Cr/Au (7/70 nm) layers are deposited thermally and patterned by the photolithography process for serpentine-shaped interconnections. Additional spin coating forms the top polymeric passivation layer. Final patterning and dry etching steps complete the fabrication of stretchable electronic devices.

2.3. Fabrication of gecko-inspired miniaturized-pillar structure

Miniaturized-pillar (m-pillar) structures, inspired by gecko setae, were fabricated through a combination of photo-/soft-lithography techniques. Photolithography and inductively-coupled-plasma-assisted deep-reactive-ion-etching patterned an array of holes (reverse structure of m-pillar) on Si wafer. Each hole pattern in this Si master has the size of 1 μm diameter and 3 μm depth. The negative replica mold of m-pillars was fabricated with the photo-curable poly(urethane acrylate) (PUA; MINS 301 RM, Minuta Tech., Korea). To reduce the interfacial energy, FOTCS surface modification was performed. Stretchable electronic devices were transferred onto the fully cured bottom PDMS layer (sylgard 184, Dow Corning, USA) (1.6 MPa) on poly(vinylalchol) (PVA; Kuraray, Japan) film. Another top PDMS layer (1.6 MPa) was spin-coated and partially cured at 70°C oven. The negative pillar mold was laminated on the partly cured PDMS, pressed, and then completely cured in 70°C oven. The final m-pillars were formed by removing the mold.

2.4. Fabrication of mSC electronic patch

The electronics were released from the temporary handling substrates by etching a sacrificial layer, and then transferred onto an elastomer film of ~39 kPa modulus (Ecoflex 0030, Smooth-on Inc., USA) coated on a PVA film (water-dissolvable temporary supporting layer). After super-hydrophobic treatment of the mSC mold, three PDMS prepolymer solutions diluted by toluene (concentrations: 0.5 g/mL, 1 g/mL, and 2 g/mL) were mixed with the PDMS curing agent of 0.1 g/mL concentration, respectively. The resulting PDMS mixture solutions were then spin-coated in the mSC mold in a sequential order, following spin coating of ~39 kPa PDMS. The coated film was partially cured in 70°C oven and assembled with O_2-plasma-treated devices on Ecoflex/PVA film. The assembled sample was strongly pressed with ~5 mm thick PDMS dampers to equally distribute the applied pressure. Full curing (in 70°C oven), followed by detaching the mSC mold completed the fabrication steps. Additional electrodes for electrophysiology monitoring and iontophoresis were transfer-printed onboard the mSC structure with water soluble tapes (3M Corp., USA).

2.5. Adhesion tests and verification of conformal contacts

The patch adhesive was characterized on a human skin mold (PUA duplication with human skin morphology). Patch samples with different surface structures (gradual mSC, m-pillar, 1.2 MPa mSC, 60 kPa flat) were utilized and back-supported by ~50 μm thick PET films coated with 10:1 PDMS. Each sample was cut into ~1.2 cm width and the adhesion force (maximum force during dragging) was measured by a digital force gauge (Mark-10, USA). Conformal contact was verified by using the mSCs/m-pillar patches containing fluorescent dyes (rubrene, Sigma Aldrich, USA). The patches were laminated on artificial Ecoflex skin segments, and the three-dimensional interface between the patch and the skin

was observed via confocal microscopy (LSM780 NLO, Carl Zeiss, Germany).

2.6. Characterization of mechanical properties (system modulus)

After dissolving the PVA film (water-dissolvable temporary supporting layer), the patch was rolled up. Both ends of the rolled patch were fixed by the digital force meter, which measured the induced load during stretching. The system modulus was calculated from the slope of stress-strain curves. To characterize the modulus of the entire system stack, similar experiments were performed across various elastomers (e.g. PDMS, Ecoflex).

2.7. Procedures for reuse of mSC patches

The mSC patch laminated on the skin was detached by the water-soluble tape which acted as a temporary substrate. After cleansing the patch with acetone (the ingredient of the nail manicure remover) and reloading drugs by drop-casting the drug solution, the patch was re-attached onto the skin. Then the water-soluble tape was easily removed from the skin with the water. Following drying step finished the patch regeneration (Movie S3).

2.8. Monitoring human vital signs *in-vivo* and acute disease model

The connector consisted of an array of metal lines was interconnected to a data-acquisition system (National Instruments, USA) through an anisotropic conductive film. Devices were attached on a few locations on skin, including the radial artery, joint, and chest. After the PVA film was dissolved, the patch made conformal contacts to monitor highly

sensitive physiological signals. For animal disease models, strain gauges attached on the epidermis over the heart of the mouse measured the heart rate and respiratory rate. The ethanol tap on the mouse body was utilized to induce acute hypothermia.[S4] 100 μg Norepinephrine (Sigma Aldrich, USA) and 100 μg propranolol (Sigma Aldrich, USA) diluted with phosphate buffered solution were intravascular injected to cause and alleviate acute hypertensive emergency.[S5] Injection of desire-sized thrombus which was formed from mouse blood into inferior vena cava led to blocking pulmonary capillary (pulmonary thromboembolism). [S6]

2.9. Wireless communication system

The custom-made wireless communication system equipped on the smart band was built. It consists of a controller, Bluetooth unit (Arduino Pro Mini, Sparkfun, USA), and battery (Figure S3a). The medical devices on mSC patches were connected to the external commercial devices (e.g. tablets or smartphones) wirelessly through Bluetooth module of the smart band. Data was transferred to external devices from mSC patches and commands were delivered vice versa. For instance, the resistance change of strain gauges was measured through the specially designed resistor-capacitor (RC) circuit (Figure S3b). The resistance alternation modulated the discharging time of capacitor, which was detected by the controller unit and wirelessly transferred to external devices through Bluetooth unit. A Labview (National Instruments, USA) program analyzed the RC delay and changed over to original resistance values. The program also monitored the motion of high-risk patients, such as tremors, and sent alarms in emergency situations (Movie S1). Another program installed in controller unit can remotely turn on/off the iontophoresis actuator by using smartphone

applications (SPLDuino Lite, Helloapps, USA) (Movie S2).

2.10. Synthesis of RITC-doped mesoporous silica nanoparticles with enlarged nanopores

44 μL of 3-aminopropyltriethoxysilane (APTES; Aldrich, USA), 10 mg of rhodamine B isothiocyanate (RITC; Aldrich, USA), and 1 mL of anhydrous ethanol (Aldrich, USA) were mixed and stirred overnight under the dark condition. Amine group in APTES and isothiocyanate group in RITC were covalently conjugated. The solution was stored in the refrigerator and used without further purifications. To synthesize RITC-doped mesoporous silica nanoparticles with enlarged nanopores (RITC-MSN-L), previous method[S7] was adopted and modified. In details, 3 g of hexadecyl trimethyl ammonium chloride solution (CTAC, 25 wt% in water; Aldrich, USA), 90 mg of triethanolamine (Samchun, Korea), and 30 mL of deionized water were mixed. The solution was heated to 95°C with vigorous stirring. After 1 hour, 2.5 mL of trimethylbenzene (TMB; Aldrich, USA) was added and 2.25 mL of tetraethylorthosilicate (TEOS; Acros, USA) and 225 μL of RITC-APTES solution were injected simultaneously. The resulting solution was aged for another 1 hour. The products were centrifuged and washed for several times with deionized water and ethanol to remove unreacted precursors, and dispersed in ethanol. To remove the template (hexadecyl trimethyl ammonium cation in mesopores), 500 μL of HCl (35%; Samchun, Korea) was added and stirred at 60°C for 1 hour. Then, products were centrifuged and washed by anhydrous ethanol for several times and redispersed in anhydrous ethanol (25 mL). To functionalize RITC-MSN-L with amine groups, 100 μL of APTES was added to ethanol solution containing RITC-MSN-L. To accelerate the reaction, the mixture was refluxed for 3 hours. After the centrifugation and washing with anhydrous ethanol, amine-functionalized RITC-MSN-L was

redispersed in 10 mL of anhydrous ethanol. PEG was covalently conjugated onto RITC-MSN-L-NH2. 100 mg of mPEG-SG 5000 (Succinimidyl glutarate terminated; Sunbio, Korea) was added to RITC-MSN-L-NH2 solution and stirred overnight at 35◦C. After reaction was completed, products were centrifuged and washed with ethanol and redispersed in 10 mL of chloroform.

2.11. Immunofluorescence and western blot analysis

The skin tissues were embedded in optimal cutting temperature (OCT) compound and were sliced at coronal plane to 10 μm thick by microtome (Leica, Germany). This sliced tissues were mounted on slides, and stained with Hematoxylin-Eosin (MHS16, HT110180, Sigma aldrich, USA) by standard histochemical procedure. For the Figure S7c, the H&E staining of mouse skin was immediately performed after detaching the laminated patches.

Moreover, to prepare immunofluorescence imaging of inflammation factors, we utilized IL-1β (SC-7884, Santa Cruz Biotechnology, USA) and iNOS (2982S, Cell Signaling Technology, USA) by standard protocol. For the western blot, lysates of skin tissue were prepared with Lysis buffer, which were made of 150 mM NaCl, 50 mM Tris-HCl (pH 7.4), 1% NP-40, 0.1% Sodium Dodecyl Sulfate (SDS), 1 mM Sodium orthovanadate (Na_3VO_4), 5 mM Sodium Fluoride (NaF), 0.25% Sodium Deoxycholate, 5 mM N-Ethylmethylamine, and protease inhibitor cocktail (Roche, Switzerland). The protein concentration was determined with BCA Protein Assay kit (Thermo Fisher Scientific, USA). Tissue lysate samples were separated on 4-12% Bis-Tris Plus gel (Thermo Fisher Scientific, USA) with MES buffer (50 mM MES, 50 mM Tris Base, 0.1% SDS, 1 mM EDTA, pH 7.3) and transferred to Polyvinylidene difluoride (PVDF) membrane with 0.2 micrometer pores (Bio-rad., USA).

The blots were incubated with primary antibodies: mouse anti-TNFα (1:500, Abcam, USA), mouse anti-IL-1β (1:500, Cell Signaling Technology, USA), and mouse-anti β-actin (1:20000, Sigma, USA). After that, all blots were incubated with secondary antibody: goat anti-mouse IgG-HRP (Santa Cruz Biotechnology, USA). The blot images were captured using the Fusion FX7 system (Vilber Lourmat, Germany) and band density was analyzed by Bio-1D program (Vilber Lourmat, Germany).

2.12. Laboratory animals

Balb/c nude mice (age: 6 weeks) were obtained from the Experimental Animal Center, Chuncheon Center, Korea Basic Science Institute (KBSI), Chuncheon, South Korea. These animals were individually housed in transparent plastic cages with wire grid covers under controlled temperatures (22-24◦C) with the 12 hour light/dark cycle (lights on from 08:00 to 20:00). All animal procedures were in accordance with the Guide for the Care and Use of Laboratory Animals issued by the Laboratory Animal Resources Commission of KBSI. The Institutional Animal Care and Use Committee at the KBSI (KBSI-AEC1409) reviewed and approved this study. All of the experiments were conducted to minimize the number of animals used and the suffering caused by the procedures used in the current study.

3. Supporting References

[S1] J. D. Eshelby, *Proc. R. Soc. A* **1957**, *241*, 376.

[S2] R. H. LaMotte, S. G. Shimada, P. Sikand, *Exp. Dermatol.* **2011**, *20*, 778.

[S3] S. G. Shimada, R. H. LaMotte, *Pain* **2008**, *139*, 681.

[S4] W. C. M. Cramer, G. P. Toorop, *Gen. Pharmacol.* **1998**, *30*, 195.

[S5] J. Polio, C. C. Sieber, E. Lerner, R. J. Groszmann, *Hepatology* **1993**, *18*, 128.

[S6] M. H. Todd, J. B. Forrest, D. B. J. Cragg, *Am. Heart J.* **1983**, *105*, 769.

[S7] L. Pan, Q. He, J. Liu, Y. Chen, M. Ma, L. Zhang, J. Shi, *J. Am. Chem. Soc.* **2012**, *134*, 5722.

4. Supporting Figures

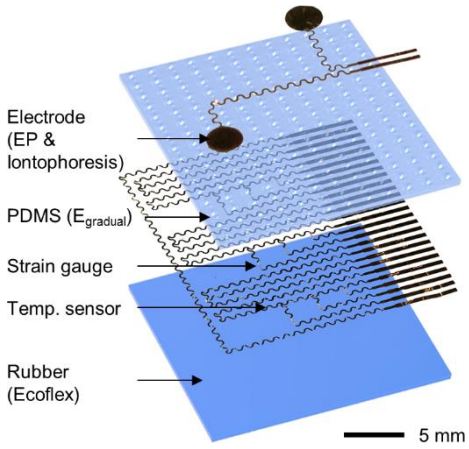

Figure S1. Exploded view of mSC electronic patch. The strain gauge and temperature sensor array (image in the middle) is embedded between silicone rubber (Ecoflex; cartoon at the bottom) and top mSCs structured elastomer layer (PDMS; cartoon at the top). The electrodes (topmost image) are located on the surface of the electronic patch.

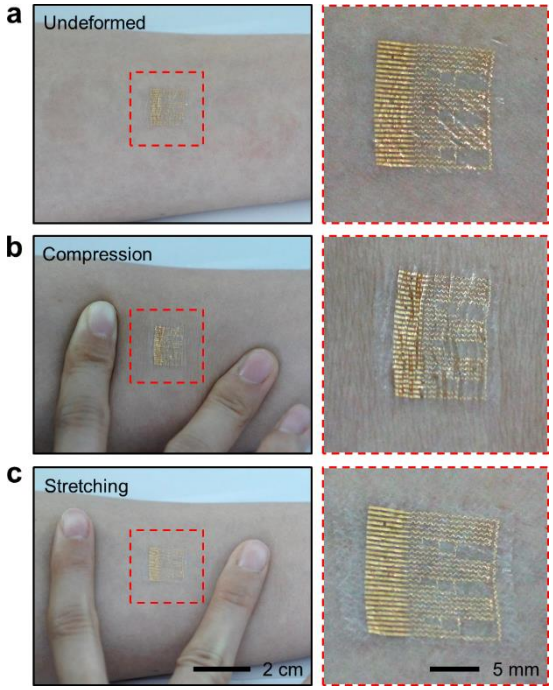

Figure S2. a-c, The mSCs electronic patch laminated on skin: undeformed (**a**), compressed (**b**), and stretched (**c**) states. Photographs (right column) show magnified view of each state in the red dotted box.

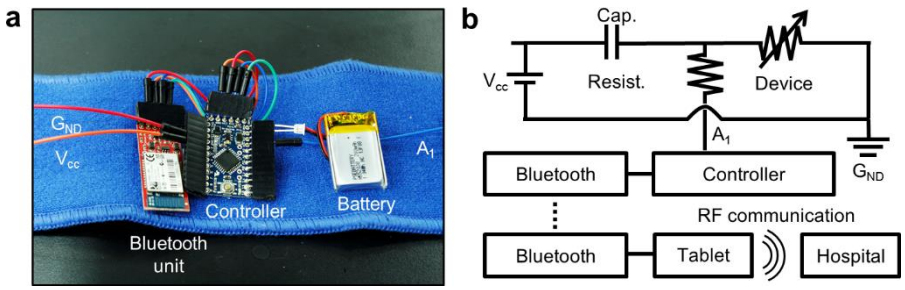

Figure S3. a, Image of a custom-made smart band that consists of a Bluetooth unit, a battery, and a controller unit. **b,** Schematic diagram of the smart band circuit for the real time sensing, wireless data transfer to external devices, and remote control of the electronics in the patch using commercial devices such as a smartphone.

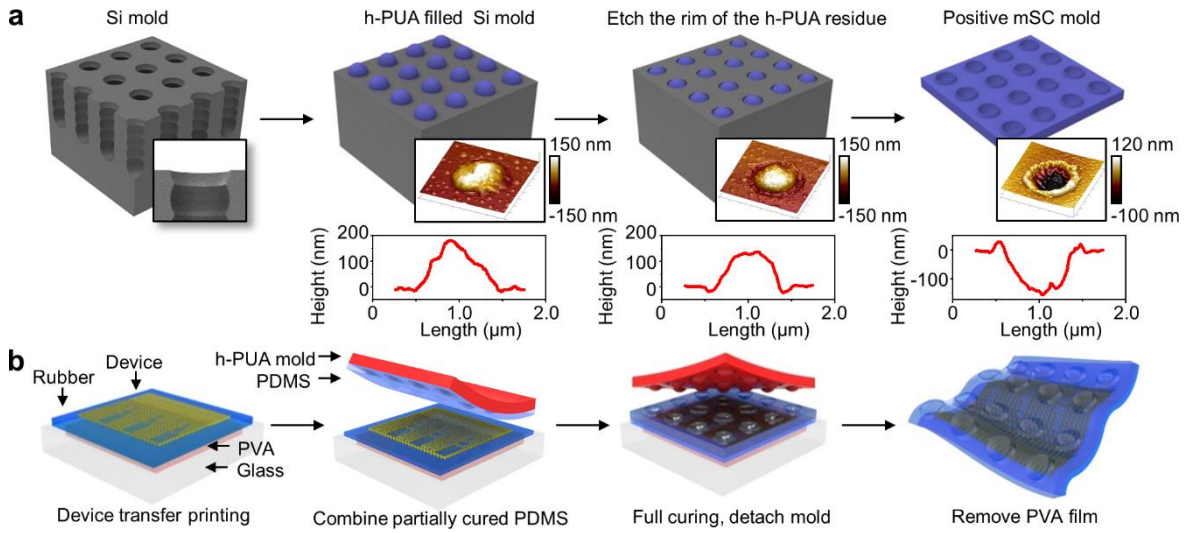

Figure S4. a, Schematic diagram for the fabrication of mSCs mold. The UV curable h-PUA is poured in the sinuous hole-patterned Si mold, partially cured, and detached leaving residual embossed h-PUA on the Si mold. The rim of the embossed h-PUA is etched with oxygen plasma. Repetitive molding makes positive mSCs mold. The insets show the 3D AFM images and corresponding two dimensional AFM profile of the vertical cross-section, respectively. **b,** Schematic illustration of electronic patch fabrication steps with gradual modulus mSCs.

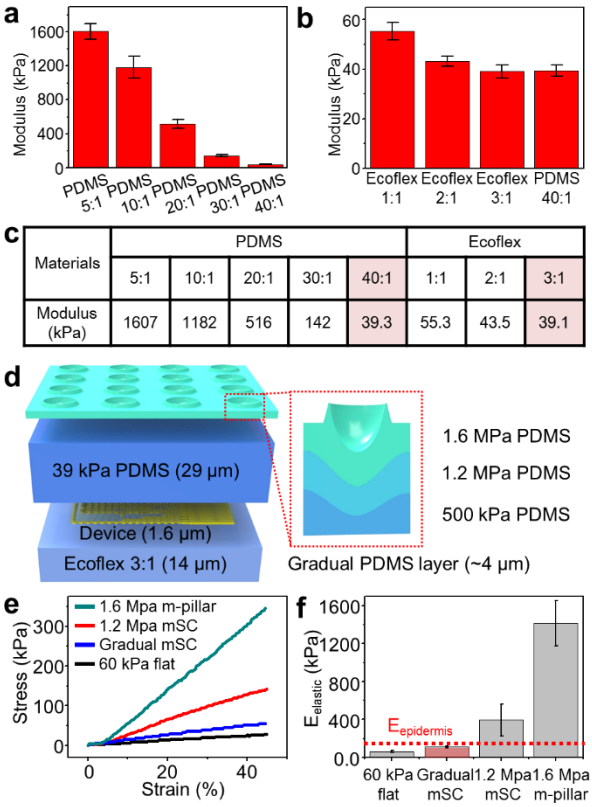

Figure S5. a, Change of the Young's modulus of PDMS as the ratio of prepolymer to curing agent is varied. The more prepolymer gives rise to lower modulus. The ratio in the x axis denotes the weight ratio of prepolymer : curing agent. **b,** Change of the Young's modulus of Ecoflex (silicone rubber) as the ratio of prepolymer to curing agent is varied. **c,** Table that summarizes the Young's modulus of various elastomers (PDMS and Ecoflex). **d,** Schematic illustration of the exploded view of the mSC electronic patch. The dashed red box shows a magnified illustration of the mSC structure. The mSC structure consists of three elastomeric layers with gradually changing modulus. The thickness of the gradual PDMS layer is less than ~4 μm. **e,** Stress-strain curves for different layers of elastomeric patch. **f,** Comparison of the system modulus of various elastomeric patch layers. Red dotted line shows the modulus of human epidermis.

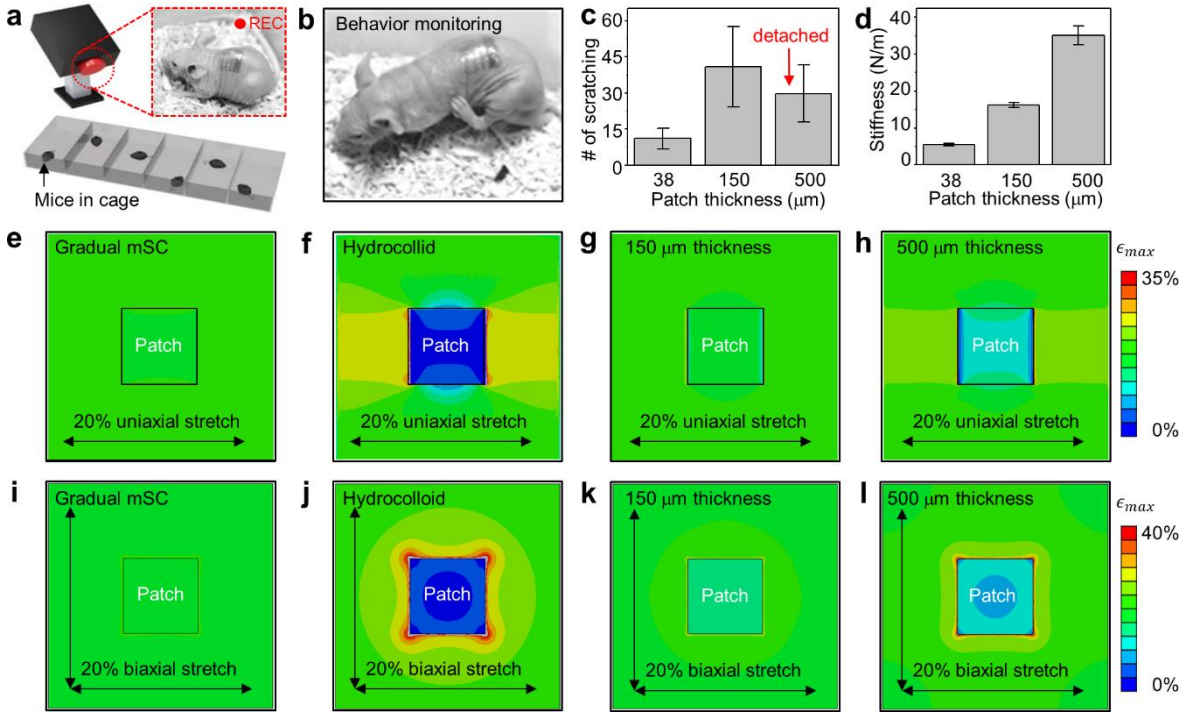

Figure S6. a, Schematic illustration of the animal behavior observation. Scratching numbers are counted to quantify the degree of discomfort. **b,** Photograph of mouse's scratching. **c,** The number of scratching with different patch thicknesses. The scratching number of ~500 μm thick patch decreases below that of ~150 μm thick patch, because the patch was delaminated from the back of mice before the experiment is over. **d,** Stiffness versus patch thickness. **e-h,** Finite element modeling of the load on the patch-attached skin when ~20% uniaxial stretch is applied (~38 μm gradual mSC patch (**e**), hydrocolloid patch (**f**), mSC patch with thickness ~150 μm (**g**) and ~500 μm (**h**), respectively). **i-l,** FEM simulation of the induced strain on the patch-attached skin when ~20% biaxial strain is applied; result of ~38 μm gradual mSC patch in (**i**), hydrocolloid patch in (**j**), ~150 μm mSC patch in (**k**), and ~500 μm mSC patch in (**l**), respectively.

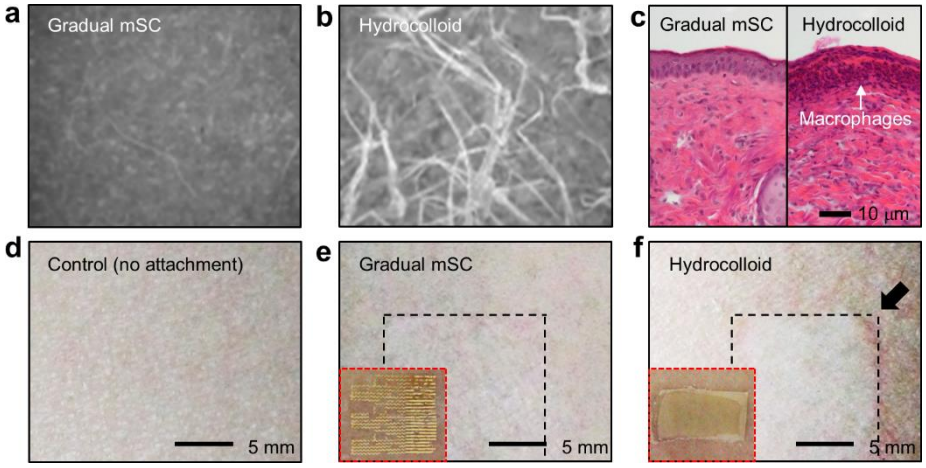

Figure S7. a and **b,** Microscope images show the surface of patches (gradual mSC patch in (**a**) and hydrocolloid patch in (**b**)) after peeling-off. **c,** Cross section image of the skin in the H&E stain histology. (left: gradual mSC patch, right: hydrocolloid patch). **d-f,** The skin conditions after detaching each patch from human arms: control (no attachment) (**d**), gradual mSC patch (**e**), and hydrocolloid patch (**f**). Each patch is laminated on skin for 4 days. The reddish irritation is observed on the hydrocolloid-laminated skin (black arrow in (**f**)). The insets of (**e**) and (**f**) present the condition of the laminated patches on the skin after attaching for 4 days.

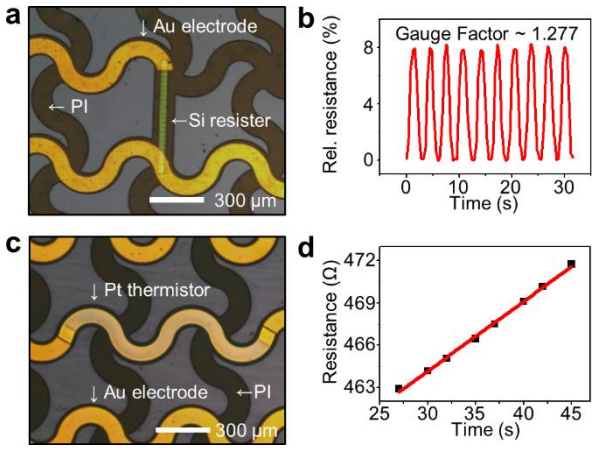

Figure S8. **a,** Microscope image of the Si strain gauge. **b,** The relative resistance changes of the strain gauge by externally applied strains. The gauge factor is ~1.277. **c,** Microscopic image of the Pt thermistor-based temperature sensor. **d,** The calibration curve of the temperature sensor.

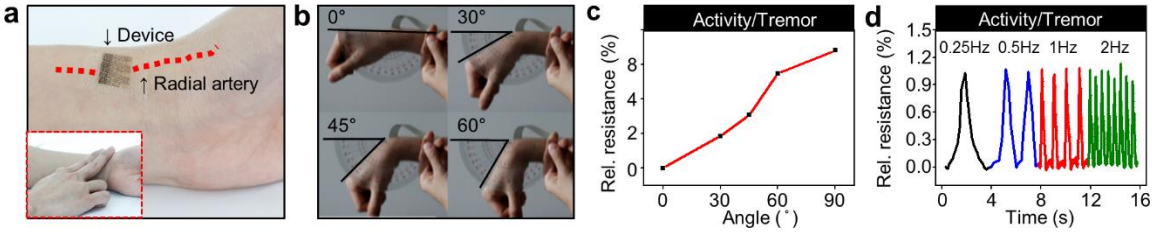

Figure S9. a, Image of the pulse measurement by using the mSC electronic patch on the radial artery. Inset shows conventional tactile diagnosis method for the pulse measurement on the radial artery. By applying the external pressure on the pulse-measuring finger tips, the more sensitive pulse measurement can be done. **b,** Images of the wrist movements with different angles from 0° to 60°. **c,** Simultaneously measured strain during motions of (**b**). **d,** Monitoring the joint movements of the wrist as frequencies vary from 0.25 Hz to 2 Hz.

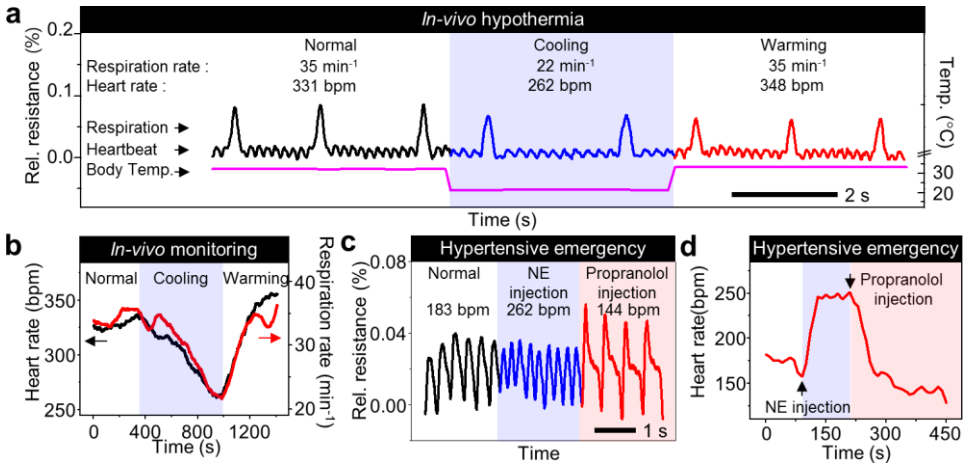

Figure S10. a and **b,** Continuous monitoring of vital signs (e.g. respiration, heartbeat, and body temperature) in a mouse disease model of hypothermia induced by ethanol tap and treated with warming (**a**). Change in heart rate and respiration rate at whole time range (**b**). **c** and **d,** Continuous monitoring of heart rate in a mouse experimental model of hypertensive emergency (**c**), which was induced by intravenous (IV) injection of norepinephrine (NE) and was sequentially treated with IV administration of propranolol (**d**).

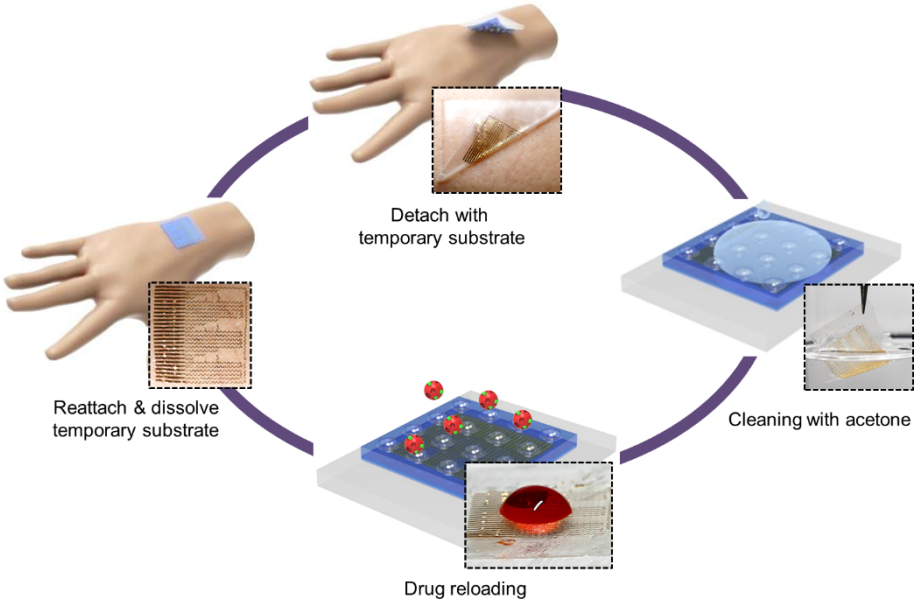

Figure S11. Schematic illustration of the regeneration of the mSC patches. The insets show photographs of each procedure.

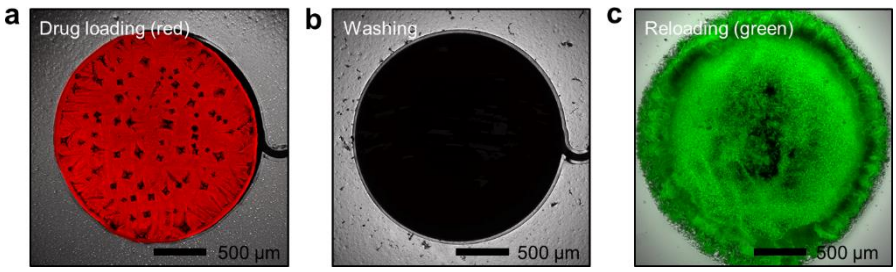

Figure S12. a-c, Drug reloading procedure onto the electrode of the mSC patch. The confocal images show that two different dyes (red: doxorubicin (**a**), green: DPA (**c**)) are successively loaded on the clean, reused electrode (**b**).

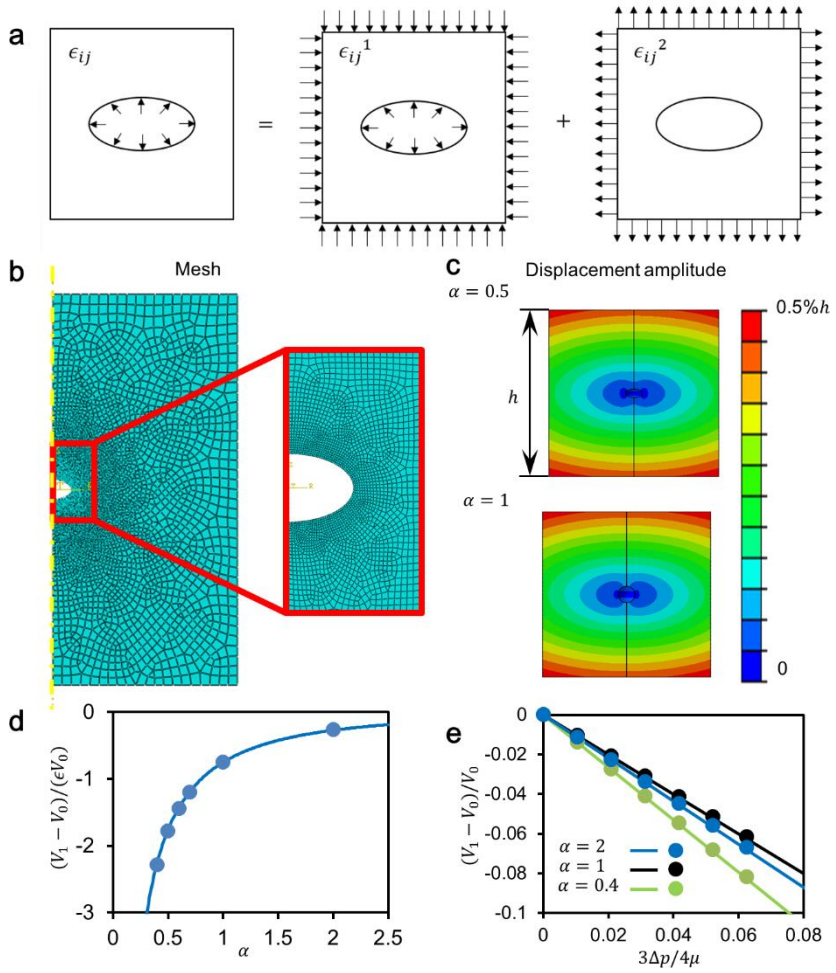

Figure S13. a, A void embedded in a body with pressure exerted on the void surface can be considered as the superposition of the following 2 configurations: both the void and the body surfaces are loaded by the same pressure; only the body surface is loaded by the pressure but in the opposite way. **b,** The mesh of the FEM model to check how the spheroid void embedded in an axisymmetric body changes. **c,** The contour plot of displacement amplitude for $\alpha = 0.5$ and 1 respectively. **d** and **e,** The comparison between the FEM results and the theoretical results where the dots are all FEM results and the curves are obtained from equation (1) in (**d**) and equation (3) in (**e**). The applied compressive strain, ϵ, is 1%.